(This is a sample cover image for this issue. The actual cover is not yet available at this time.)

International Journal of Heat and Mass Transfer 55 (2012) 3763–3773

Contents lists available at SciVerse ScienceDirect

International Journal of Heat and Mass Transfer

journal homepage: www.elsevier.com/locate/ijhmt

Numerical analysis of coupled effects of pulsatile blood flow and thermal relaxation time during thermal therapy

Tzu-Ching Shih [a,*], Tzyy-Leng Horng [b,*], Huang-Wen Huang [c], Kuen-Cheng Ju [d], Tzung-Chi Huang [a], Po-Yuan Chen [e], Yung-Jen Ho [a], Win-Li Lin [f]

[a] Department of Biomedical Imaging and Radiological Science, China Medical University, Taichung 40402, Taiwan
[b] Department of Applied Mathematics, Feng Chia University, Taichung 40724, Taiwan
[c] Department of Innovative Information and Technology, Division of Software Engineering, Langyang Campus, Tamkang University, I-lan 26247, Taiwan
[d] Department of Biomedical Engineering, I-Shou University, Kaohsiung 82445, Taiwan
[e] Department of Biological Science and Technology, China Medical University, Taichung 40402, Taiwan
[f] Institute of Biomedical Engineering, College of Medicine and College of Engineering, National Taiwan University, Taipei 10051, Taiwan

ARTICLE INFO

Article history:
Received 24 October 2011
Accepted 22 February 2012

Keywords:
Pulsatile blood flow
Thermal relaxation time
Pennes bioheat transfer equation
Wave bioheat transfer equation
Multi-block Chebyshev pseudospectral method

ABSTRACT

The main purpose of this study is to investigate the coupled effects of the pulsatile blood flow in thermally significant blood vessels and the thermal relaxation time in living tissues on temperature distributions during thermal treatments. Considering the fact that propagation speed of heat transfer in solid tissues is actually finite according to experiments, the traditional Pennes bioheat transfer equation (PBTE) was modified to a wave bioheat transfer equation (WBTE) that contains both wave transportation and diffusion competing with each other and characterized by the thermal relaxation time. The wave behavior will be more dominant when the relaxation time is large. WBTE together with a coupled energy transport equation for blood vessel flow was used to describe the temperature evolution of our current tumor–blood vessel system, and the equations were numerically solved by the highly accurate multi-block Chebyshev pseudospectral method. Numerical results showed that temperature evolution from WBTE was quite different from their counterparts from PBTE due to the dominant wave feature under large relaxation time. For example, larger relaxation time would preserve high temperature longer and this effect is even more pronounced when heating is fast. It further implies that heat is drained more slowly when relaxation time is large, and would make thermal lesion region cover the tumor tissue, the heating target, better. This phenomenon would therefore hint that the traditional PBTE simulations might under-estimate the thermal dose exerted on tumor. As to the pulsation frequency of blood flow from heart beat which was originally predicted to be important here, it turned out that the thermal behavior is quite insensitive to pulsation frequency in the current study.

1. Introduction

Heat transfer in living tissues is a key issue to thermal therapies. Thermal therapy uses elevated temperatures to kill tumor cells for therapeutic purposes [1–3]. Thermal coagulation necrosis occurs when a biological tissue is heated beyond the threshold temperature of protein thermal denaturation for a few seconds [4–6]. Depending on the tissue types, the heat-induced denaturation starts when temperature is higher than 55 °C [5]. The tissue temperature can be raised by various methods, such as high-intensity focused ultrasound [7], radiofrequency ablation [8], microwave ablation [9], and laser surgery [10–11]. Furthermore, temperature distribution in a living tissue mainly depends on heat conduction through tissue, heat convection through moving fluids that is adjacent to or within the tissue such as blood flow and interstitial fluids, heat generation by tissue metabolism, heat sink by blood perfusion and heat deposition with various patterns generated by the external heating source during thermal treatments. The well-known Pennes bioheat transfer equation (PBTE), as shown in Eq. (1), originally designed for predicting heat transfer in human forearm, is widely used for modeling the heat transfer in living tissues due to using a uniform blood perfusion term to describe heat transfer between the blood and tissue [12].

* Corresponding authors. Addresses: Department of Biomedical Imaging and Radiological Science, China Medical University, 91 Hseuh-Shih Road, Taichung 40402, Taiwan. Tel.: +886 4 22053366x7709; fax: +886 4 2208 1447 (T.-C. Shih), Department of Applied Mathematics, Feng Chia University, 100 Wen-Hwa Road, Seatwen, Taichung 40724, Taiwan. Tel.: +886 4 2451 7250x5126; fax: +886 4 2451 0801 (T.-L. Horng).

E-mail addresses: shih@mail.cmu.edu.tw (T.-C. Shih), tlhorng@math.fcu.edu.tw (T.-L. Horng).

0017-9310/$ - see front matter © 2012 Elsevier Ltd. All rights reserved.
doi:10.1016/j.ijheatmasstransfer.2012.02.069

Nomenclature

c_b	specific heat of blood (J kg^{-1} K^{-1}), c_b = 3770 J kg^{-1} K^{-1}
c_t	specific heat of solid tissue (J kg^{-1} K^{-1}), c_t = 3770 J kg^{-1} K^{-1}
c_0	coefficient in Eq. (5), $c_0 = -\frac{8\mu\bar{w}}{r_0^2}$
c_1	coefficient in Eq. (5)
$\bar{c}_j$	coefficient in Eq. (22)
d	diameter of blood vessel (mm), $d = 2r_0$
D	collocation derivative matrix, referring to Eq. (24), $D_{ij} = l_j'(x_i)$
EM_{43}	thermal dose or equivalent minutes at 43 °C
$f(x)$	single-variable function, referring to Eq. (21)
$f_N(x)$	Nth degree interpolation polynomial approximating $f(x)$ in Eq. (21)
fac	coefficient of relative intensity of pulsation in a blood vessel, $fac = \frac{c_1}{c_0}$
J_0	the Bessel function of the first kind of order zero, referring to Eq. (10)
k	thermal conductivity (W m^{-1} K^{-1}), referring to Eqs. (2) and (3)
k_b	thermal conductivity of blood (W m^{-1} K^{-1}), k_b = 0.5 W m^{-1} K^{-1}
k_t	thermal conductivity of tissue (W m^{-1} K^{-1}), k_t = 0.5 W m^{-1} K^{-1}
$l_j(x)$	Lagrange interpolation polynomial, referring to Eq. (22)
N	degree of interpolation polynomial, referring to Eq. (21)
N_x	degree of interpolation polynomial in x direction, referring to Eq. (26)
N_y	degree of interpolation polynomial in y direction, referring to Eq. (26)
p	pressure (kg m^{-2})
q	heat flux (W m^{-2})
r	radial component of cylindrical coordinates (mm)
$\vec{r}$	position vector
r_0	radius of blood vessels (mm), r_0 = 1 mm here
r_1	boundary limit of tumor in r direction (mm), r_1 = 5 mm here
r_{max}	boundary limit of computational domain in r direction (mm), $r_{\max}$ = 10 mm here
R	factor in Eq. (29)
t	time (s)
t_h	heating duration (s)
t_f	upper limit of integral in Eq. (29) (s)
Q	time-average heating power density listed in Table 2 (W cm^{-3})
$\dot{Q}_{avg}$	average volume flow rate of blood flow (mm^3 s^{-1})
Q_b	heating power density in blood vessel (W cm^{-3})
$\tilde{Q}_b$	time average of Q_b (W cm^{-3})
Q_m	rate of tissue metabolic heat generation (W cm^{-3})
Q_t	heating power density in tumor (W cm^{-3})
$\tilde{Q}_t$	time average of Q_t (W cm^{-3})
T	temperature (K)
$\tilde{T}$	period of time of heart beat (s)
T_a	temperature of arterial blood and ambient temperature (K), T_a = 310 K
T_b	temperature of blood flow (K)
T_N	Nth order Chebyshev polynomial
T_t	temperature of solid tissue (K)
w	steady component of axial velocity (mm s^{-1}), referring to Eqs. (4) and (6)
$\bar{w}$	averaged velocity (mm s^{-1}), referring to Eq. (8) and Table 1
w_1	coefficient in Eq. (6)
W	axial velocity (mm s^{-1}), referring to Eq. (6)
W_b	blood perfusion rate (kg m^{-3} s^{-1}), W_b = 0.5 kg m^{-3} s^{-1}
x_j	Chebyshev–Gauss–Lobatto collocation points, referring to Eq. (21)
z	axial component of cylindrical coordinates (mm)
z_1	lower boundary limit of tumor in z direction (mm), z_1 = 5 mm here
z_2	upper boundary limit of tumor in z direction (mm), z_2 = 15 mm here
z_{max}	upper boundary limit of the computational domain in z direction (mm), $z_{\max}$ = 100 mm here

Greek symbols

α	Womersley number, $\alpha = \frac{r_0}{\sqrt{\nu/\omega}}$
μ	dynamic viscosity of blood (Pa · s = kg m^{-1} s^{-1}), $\mu = 4 \times 10^{-3}$ Pa · s
ρ_b	density of blood (kg m^{-3}), ρ_b = 1,050 kg m^{-3}
ρ_t	density of solid tissue (kg m^{-3}), ρ_t = 1,050 kg m^{-3}
ν	kinematic viscosity of blood (m^2 s^{-1}), $\nu = 2.8571 \times 10^{-6}$
τ	thermal relaxation time (s)
ω	angular frequency of heart beat (s^{-1})
Ω	computational domain
Γ	interface between blood vessel and tissue, referring to Eqs. (16) and (17)

Subscripts

b	blood
t	tissue

$$\rho_t c_t \frac{\partial T_t}{\partial t} = \nabla \cdot (k_t \nabla T_t) - W_b c_b (T_t - T_a) + Q_m + Q, \quad (1)$$

with t being the time, T_t the tissue temperature, ρ_t the tissue density, c_t the tissue specific heat, k_t the tissue thermal conductivity, W_b the arterial blood perfusion rate, c_b the blood specific heat, T_a the arterial blood temperature (usually set to be same as the ambient human body temperature 37 °C), Q_m the rate of tissue metabolic heat production (usually set to 0.0001 g cal/cm s), and Q the external heat source. Pennes [12] first stated that the rate of heat transfer from blood to tissue at any point is proportional to the temperature difference between the arterial blood and tissue at that point. He also assumed the vein blood temperature to be equal to the tissue temperature. In this model, the rate of increase of tissue temperature is balanced by heat conduction through the tissue, metabolic heat generation, heating (or cooling) effects of the arterial blood supply [13–17], and external heat source. However, a fundamental criticism of Pennes model by Nelson [13] is that the treatment of blood flow term as a distributed heat source (or sink) mistakenly presumes that the capillary vasculature is the major site of heat exchange. In other words, the blood flow term is a scalar property. In fact, the blood flow in a tissue usually has a direction from artery to vein passing through the capillary bed. Furthermore, the blood and its surrounding tissues are not in thermal equilibrium when the blood vessel diameter is larger than 500 μm [18–26]. This means the energy equations for tissue and blood in significantly large vessel must be treated individually.

The cyclic heart contraction pumps blood through vascular network and form a circulatory system. This periodic pumping generates pulsatile blood flow in all arteries [27–30]. Womersley [31] investigated the periodic-in-time velocity profile for pulsatile blood flow, driven by a given oscillating pressure gradient, inside a straight circular blood vessel. Using the dimensionless Womersley number to characterize the frequency of pulsatile blood flow

in blood vessels, Loudon and Tordesillas [32] demonstrated that the flow tracks the oscillating pressure gradient tightly and the velocity profile exhibits a parabolic shape when the Womersley number is small. When the Womersley number is large, the phase lag between velocity and pressure gradient becomes larger and the velocity profile may display a shape of two peaks when oscillation amplitude of pressure is large. One of the key issues of thermal treatments is blood flow. Blood flow usually drains the delivered heat from the heating region which causes insufficient thermal dose in the targeted volume. This is an important factor needed to be considered carefully in thermal treatments [33–36]. In fact, the differential therapeutic effect of thermal treatments between malignant and normal tissue may primarily depend on the vascular characteristics of the tumor [37]. Craciunescu and Clegg [38] solved the fully coupled Navier–Stokes and energy equations to obtain the temperature distribution of pulsatile blood flow within a rigid blood vessel. They found that the reversed flow enhances as the Womersley number becomes larger, which results in a smaller temperature difference between forward and reverse flows. Nevertheless, in their model they only focused on the temperature distribution in blood vessels without considering the surrounding tissue. Khanafer et al. [36] and Horng et al. [39] further studied the effects of pulsatile blood flow on temperature distributions during hyperthermia by considering both the pulsatile blood flow in a blood vessel and its surrounding tissue.

The heat conduction term in PBTE is based on the classical Fourier law, which assumes that a temperature disturbance in any part of the materials leads to an instantaneous perturbation at each point of the whole. This implies that the propagation speed of thermal perturbation is infinite even if the intervening distance is very large, and causes some doubts and discussions [40–42]. Actually, non-Fourier heat conduction behavior has been observed in biomaterials with inhomogeneous inner structures [43], in biological tissues [44,45], in canine thigh muscles [46], and in processed meats [47,48]. Considering the finite propagation speed for thermal disturbance, Cattaneo [49] and Vernotte [50] formulated a modified heat flux equation, as shown in Eq. (3) with Fourier law shown in Eq. (2) for comparison.

$$q(\vec{r}, t) = -k\nabla T(\vec{r}, t), \tag{2}$$

$$q(\vec{r}, t) + \tau\frac{\partial q(\vec{r}, t)}{\partial t} = -k\nabla T(\vec{r}, t), \tag{3}$$

where T, q, k, τ are temperature, heat flux, thermal conductivity and thermal relaxation time respectively. The thermal relaxation time for biological tissues has been found typically large leading to significant non-Fourier thermal behavior. Mitra et al. [47] measured experimentally the thermal relaxation time in a processed meat and reported that τ could be as large as 16 s approximately. Kaminski [43] reported that τ ranges from 10 to 50 s in his experiment for materials with inhomogeneous inner structures. Roetzel et al. [51] also confirmed the hyperbolic behavior of thermal propagation with τ about 1.77 s in a similar experiment. Using the thermal properties of tissue and blood from some literatures, Zhang [52] computed and argued that reasonable τ should range from 0.464 to 6.825 s. He further found that the dual-phase lag phenomenon in temperature and its gradient due to the wave feature is more pronounced when blood vessel is large. The literatures mentioned above have motivated us to fully explore the coupled effect of pulsatile blood flow in large blood vessels and thermal relaxation time on the heating of tumor tissues here, from which we believe it can deliver significant contribution to thermal therapy of tumors.

2. Mathematical model and numerical method

2.1. Velocity profile of pulsatile blood flow in a circular blood vessel

In this study, we considered the pulsatile blood flow in thermally significant blood vessels (*i.e.*, larger than 200 μm in diameter) [33,35,39], with the assumptions that the blood vessel segment is straight, the vessel wall is rigid and impermeable, and the flow is incompressible and Newtonian. Considering the steady blood flow passing through a rigid vessel of inner radius r_0, the axial Hagen–Poiseuille parabolic velocity profile can be expressed as:

$$w(r) = -\frac{1}{4\mu}(r_0^2 - r^2)\frac{dp}{dz}, \tag{4}$$

where μ is the dynamic viscosity, $\frac{dp}{dz}$ the constant pressure gradient along the axial (z) direction. Since the blood flow in the cardiovascular system is periodic, the pressure gradient can not remain to be a constant any more. Here, it is modified to have an additional sinusoidal component in time shown as follows

$$\frac{\partial p}{\partial z} = c_0 + c_1 e^{i\omega t}, \tag{5}$$

where ω is the angular frequency and the associated period of time is denoted as $\tilde{T} = \frac{2\pi}{\omega}$. The real part of sinusoidal component above will describe the realistic oscillatory driving pressure gradient as $c_1\cos(\omega t)$, and likewise the imaginary part will describe the realistic oscillatory pressure gradient as $c_1\sin(\omega t)$. Then the corresponding axial velocity profile $W(r, t)$ can be expressed as

$$W(r, t) = w(r) + w_1(r)e^{i\omega t}, \tag{6}$$

in which $w(r) = -\frac{1}{4\mu}(r_0^2 - r^2)c_0$. Here, c_0 can be related to average volume flow rate over the time period $\tilde{T}$ as follows:

$$\dot{Q}_{avg} = \frac{1}{\tilde{T}}\int_0^{\tilde{T}}\int_0^{r_0} 2\pi W r dr dt = -\frac{\pi r_0^4}{8\mu}c_0. \tag{7}$$

The average velocity can be further deduced from above

$$\overline{w} = \frac{\dot{Q}_{avg}}{\pi r_0^2} = -\frac{c_0 r_0^2}{8\mu}, \tag{8}$$

and then $W(r, t)$ can then be expressed as

$$W(r, t) = 2\bar{w}\left(1 - \frac{r^2}{r_0^2}\right) + w_1(r)e^{i\omega t}. \tag{9}$$

w_1 can be further derived from the Navier–Stokes equations, and express $W(r, t)$ as follows [29],

$$W(r, t) = 2\bar{w}\left(1 - \frac{r^2}{r_0^2}\right) + \frac{ic_1 r_0^2}{\mu\alpha^2}\left[1 - \frac{J_0(\alpha\frac{r}{r_0}i^{\frac{3}{2}})}{J_0(\alpha i^{\frac{3}{2}})}\right]e^{i\omega t}, \tag{10}$$

where $\alpha = \frac{r_0}{\sqrt{\nu/\omega}}$ denotes the Womersley number describing the competition between the inertia and viscous forces; ν denotes the kinematic viscosity of blood; J_0 is the Bessel function of the first kind of order zero. If oscillatory driving pressure gradient is $c_1\cos(\omega t)$, the corresponding velocity will then be the real part of Eq. (10). If oscillatory driving pressure gradient is $c_1\sin(\omega t)$, the corresponding velocity will then be the imaginary part of Eq. (10). Here we also define $fac = c_1/c_0 = c_1/\left(-\frac{8\mu\bar{w}}{r_0^2}\right)$ and use it to characterize the relative intensity of pulsation in the blood flow. fac = 0.5 would be mostly used in current study. When the Womersley number α is large, the effect of viscosity cannot propagate far from the vessel wall, and the blood flow in the central part of a vessel acts like an inviscid flow and can be chiefly determined by the balance between the inertia force and the pressure gradient. Under this situation, the velocity profile of oscillatory component has a

rather flat-top shape at certain phases compared with parabolic profile of Poiseuille flow. When the Womersley number α is large enough, the velocity profile of oscillatory component may even display two peaks at certain phases [39,53]. Some examples of the diameters of thermally significant blood vessels and their associated average velocities are listed in Table 1 [39]. Taking the largest blood vessel considered in Table 1 (diameter = 2 mm), and varying heart beat frequency from 1 to 3 Hz suggested by [54], the velocity profiles of oscillatory component are respectively shown in Fig. 1 at selected time phases. It can be observed that, as the Womersley number increases with increasing beating frequency, the velocity profile exhibits flat-top and even two-peak behaviors.

2.2. Temperature governing equations

In this study, a simplified annular perfused tissue, consisting of tumor and normal parts, surrounding a coaxial blood vessel with pulsatile blood passing through is considered. The tumor segment surrounds part of the blood vessel and is itself surrounded by the otherwise normal tissue. The whole axis-symmetric computational domain Ω, described by cylindrical coordinates, is bounded by $r = r_{\max}, z = 0$, and $z = z_{\max}$; the blood vessel is bounded by $r = r_0$ (with $r_0 < r_{\max}$), $z = 0$, and $z = z_{\max}$; the heating target (tumor and a part of the blood vessel) is bounded by $r = r_1$ (with $r_0 < r_1 < r_{\max}$), $z = z_1$, and $z = z_2$ (with $0 < z_1 < z_2 < z_{\max}$). All the geometric configurations mentioned above are shown in Fig. 2.

The absorbed power densities for the blood and tissue are assumed to be equal to the heating power densities. Traditionally, the governing equations for the temperature evolution are PBTE shown in Eq. (11) for solid tissue and energy transport equation shown in Eq. (12) for blood flow in terms of cylindrical coordinate under axis-symmetric situation [39]:

$$\rho_t c_t \frac{\partial T_t}{\partial t} = k_t \left[\frac{1}{r} \frac{\partial}{\partial r} \left(r \frac{\partial T_t}{\partial r} \right) + \frac{\partial^2 T_t}{\partial z^2} \right] - W_b c_b (T_t - T_a) + Q_t(r,z,t), \tag{11}$$

$$\rho_b c_b \left(\frac{\partial T_b}{\partial t} + W \frac{\partial T_b}{\partial z} \right) = k_b \left[\frac{1}{r} \frac{\partial}{\partial r} \left(r \frac{\partial T_b}{\partial r} \right) + \frac{\partial^2 T_b}{\partial z^2} \right] + Q_b(r,z,t), \tag{12}$$

with symbol of notations same as before and the subscript t denoting the tissue and b the blood. Notice that in this study the tissue metabolic heat production Q_m was neglected compared with heating power. The heat sink - $W_b c_b (T_t - T_a)$ in Eq. (11) is used to describe the perfusion effect by the microvascular network of blood flow (*i.e.*, blood vessels with diameter generally less than 200 μm), while the heat transfer due to the thermally significant large blood vessel has to be separately described by Eq. (12).

By taking into account the finite thermal propagation speed in living solid tissues, we modified Eq. (11) by heat flux formula in Eq. (3), and obtained a wave bioheat transfer equation (WBTE) as shown in Eq. (13) to replace Eq. (11):

$$\rho_t c_t \left(\tau_t \frac{\partial^2 T_t}{\partial t^2} + \frac{\partial T_t}{\partial t} \right) = k_t \left[\frac{1}{r} \frac{\partial}{\partial r} \left(r \frac{\partial T_t}{\partial r} \right) + \frac{\partial^2 T_t}{\partial z^2} \right] + W_b c_b (T_a - T_t) + Q_t + \tau_t \left(-W_b c_b \frac{\partial T_t}{\partial t} + \frac{\partial Q_t}{\partial t} \right), \tag{13}$$

in which the terms in left hand side represent heat wave and heat diffusion respectively. They are competing with each other with the thermal relaxation time τ_t characterizing the strength of wave feature compared with diffusion. When $\tau_t = 0$, WBTE (Eq. (13)) will reduce to PBTE (Eq. (12)). The external heating power density Q_t in Eq. (13) and Q_b in Eq. (12) are designated as follows

$$Q_t(r,z,t) = \begin{cases} \tilde{Q}_t \frac{\pi}{2} \sin\left(\frac{\pi t}{t_h}\right), & r_0 \leqslant r \leqslant r_1,\ z_1 \leqslant z \leqslant z_2,\ 0 \leqslant t \leqslant t_h, \\ 0, & (r,z,t) \text{ otherwise}, \end{cases}$$

$$Q_b(r,z,t) = \begin{cases} \tilde{Q}_b \frac{\pi}{2} \sin\left(\frac{\pi t}{t_h}\right), & r \leqslant r_0,\ z_1 \leqslant z \leqslant z_2,\ 0 \leqslant t \leqslant t_h, \\ 0, & (r,z,t) \text{ otherwise}, \end{cases} \tag{14}$$

where $\tilde{Q}_t$ and $\tilde{Q}_b$ are the time average of Q_t and Q_b respectively, and t_h is the duration of time of heating. In current study, we let $\tilde{Q}_t = \tilde{Q}_b = Q$. Five heating schemes consisting of various combinations of Q and t_h are shown in Table 2, and were employed here to study the effect of Q and t_h. It basically features different heating speed.

The initial conditions for the blood vessel and the tissue are

Table 1
Some typical examples of blood vessel diameter and the associated average blood flow velocity.

Diameter (mm)	Average blood flow velocity in blood vessel ($\bar{w}$) (mm s^{-1})
1.0	8
1.4	10.5
2.0	20

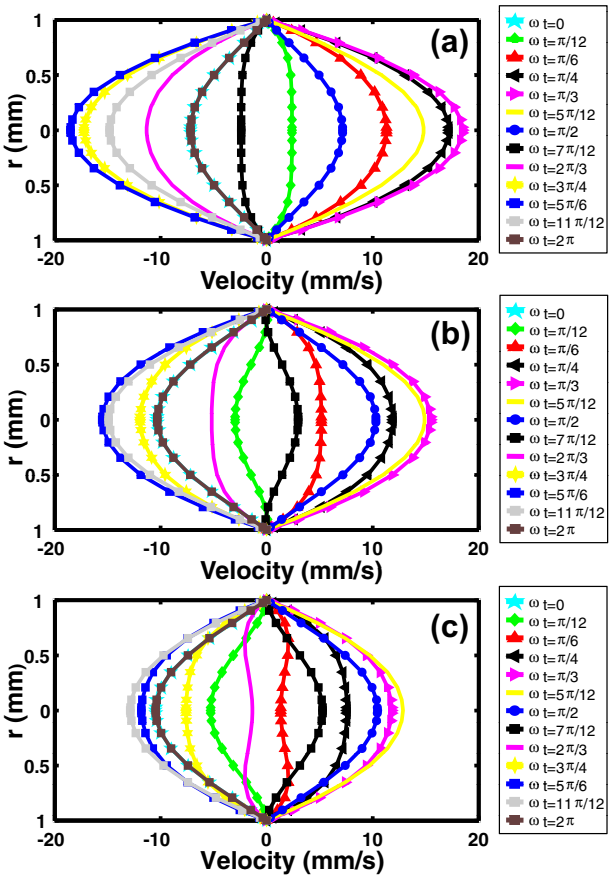

Fig. 1. Effect of Womersley number α on the oscillatory component of velocity profile for blood flow with blood vessel diameter being 2 mm. The velocity profile is shown at several selected phases between 0 and 2π for (a) $f = 1$ Hz, $\alpha = 1.2843$, (b) $f = 2$ Hz, $\alpha = 1.8162$, and (c) $f = 3$ Hz, $\alpha = 2.2244$. Flat-top and two-peak features can be observed when α is large as shown in (c). The Womersley number is calculated based on the density of blood $\rho = 1,050$ kg/m^3, and dynamic viscosity of blood $\mu = 4 \times 10^{-3}$ $Pa \cdot s$.

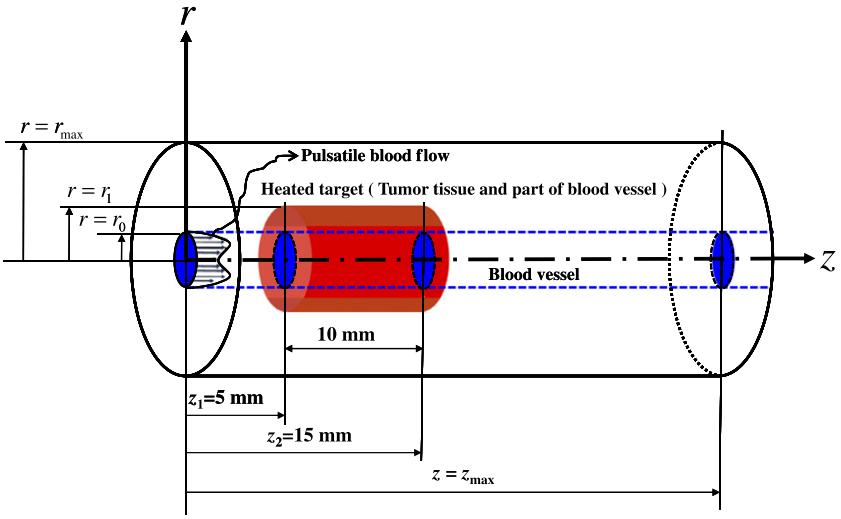

Fig. 2. Geometric configuration of coaxial tissue and blood vessel. The velocity profile of the blood vessel of radius r_0 is pulsatile as indicated. The treatment target (*i.e.*, the heating target) is specified as $z_1 \leqslant z \leqslant z_2,\ 0 \leqslant r \leqslant r_1$. This heating target includes the tumor and part of blood vessel. Here z_1 = 5 mm, z_2 = 15 mm, z_{max} = 100 mm, r_0 = 1 mm, r_1 = 5 mm, r_{max} = 10 mm.

Table 2
Parameters of the five different heating schemes featuring different heating speeds used in current study.

Heating case	I	II	III	IV	V
Time-average heating power density Q (W cm^{-3})	100	50	25	10	5
Heating duration t_h (s)	1	2	4	10	20
Total heated energy density (J cm^{-3})	100	100	100	100	100

$$T_t(r,z,0) = T_b(r,z,0) = 37\ ^\circ\mathrm{C}, \quad \text{and} \quad \frac{\partial T_t}{\partial t}(r,z,0) = 0\ ^\circ\mathrm{C/s}. \tag{15}$$

At the interface Γ $(r = r_0,\ 0 \leqslant z \leqslant z_{max})$ between the blood vessel and tissue, temperature and heat flux continuity conditions are imposed.

$$T_t = T_b \text{ at } \Gamma, \tag{16}$$

$$k_t \frac{\partial T_t}{\partial n} = k_b \frac{\partial T_b}{\partial n} \text{ at } \Gamma, \tag{17}$$

where n denotes the direction normal to Γ. At r = 0, the pole condition was applied for the blood vessel:

$$\frac{\partial T_b}{\partial r} = 0. \tag{18}$$

The boundary conditions at $r = r_{max},\ z = 0$, and $z = z_{max}$ are all set to

$$T_t = T_b = 37\ ^\circ\mathrm{C}, \tag{19}$$

except that the convective boundary condition is employed for the blood vessel part at $z = z_{max}$:

$$\frac{\partial T_b}{\partial t} + W\frac{\partial T_b}{\partial z} = 0, \quad \text{at } z = z_{max}. \tag{20}$$

Eqs. (12), (13), (15)–(20) form a well-posed partial differential initial/boundary value problem, and were solved numerically by the multi-block Chebyshev pseudospectral method shown below.

2.3. Numerical method

Eqs. (12), (13), (15)–(20) are computed here under the framework of method of lines (MOL). We first semi-discretize Eqs. (12), (13), (15)–(20) in space only, and form a system of ordinary differential and algebraic equations (ODAE) that can be further integrated in time by many well-developed ODAE solvers. Here, we spatially discretize Eqs. (12), (13), (15)–(20) by the highly accurate multi-block Chebyshev pseudospectral method, and then integrate the resultant ODAE system by an efficient MATLAB index-1 ODAE solver ode15s. The ordinary differential equations in the resultant semi-discrete system are from the spatial discretization of Eqs. (12), (13), (20) which are time dependent, and the algebraic equations are from the rest boundary and interface conditions which are time-independent. Ode15s is an explicit variable-order and variable-step-size (VSVO) ODAE solver. It can adjust the step size and order of scheme automatically during integration to meet

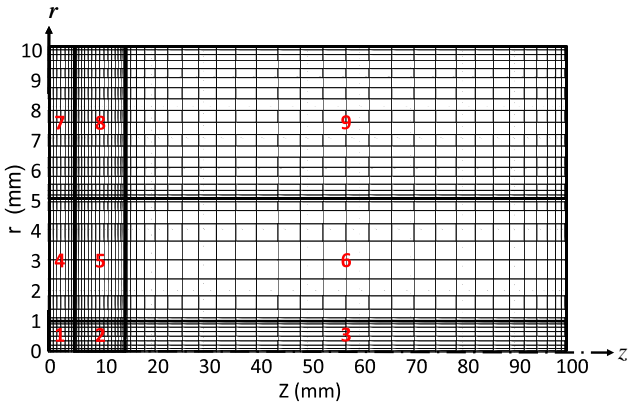

Fig. 3. The overall computational domain is decomposed into 9 rectangular blocks in r–z coordinates. Notice that blocks 1–3 are for the blood vessel, and blocks 4–9 are for the tissue with block 5 being the tumor and the others being the normal tissue. Heating zone indicated in Fig. 1 would be blocks 2 and 5. Grids are clustered more densely near boundary/interface in each block due to the property of Chebyshev–Gauss–Lobatto mesh.

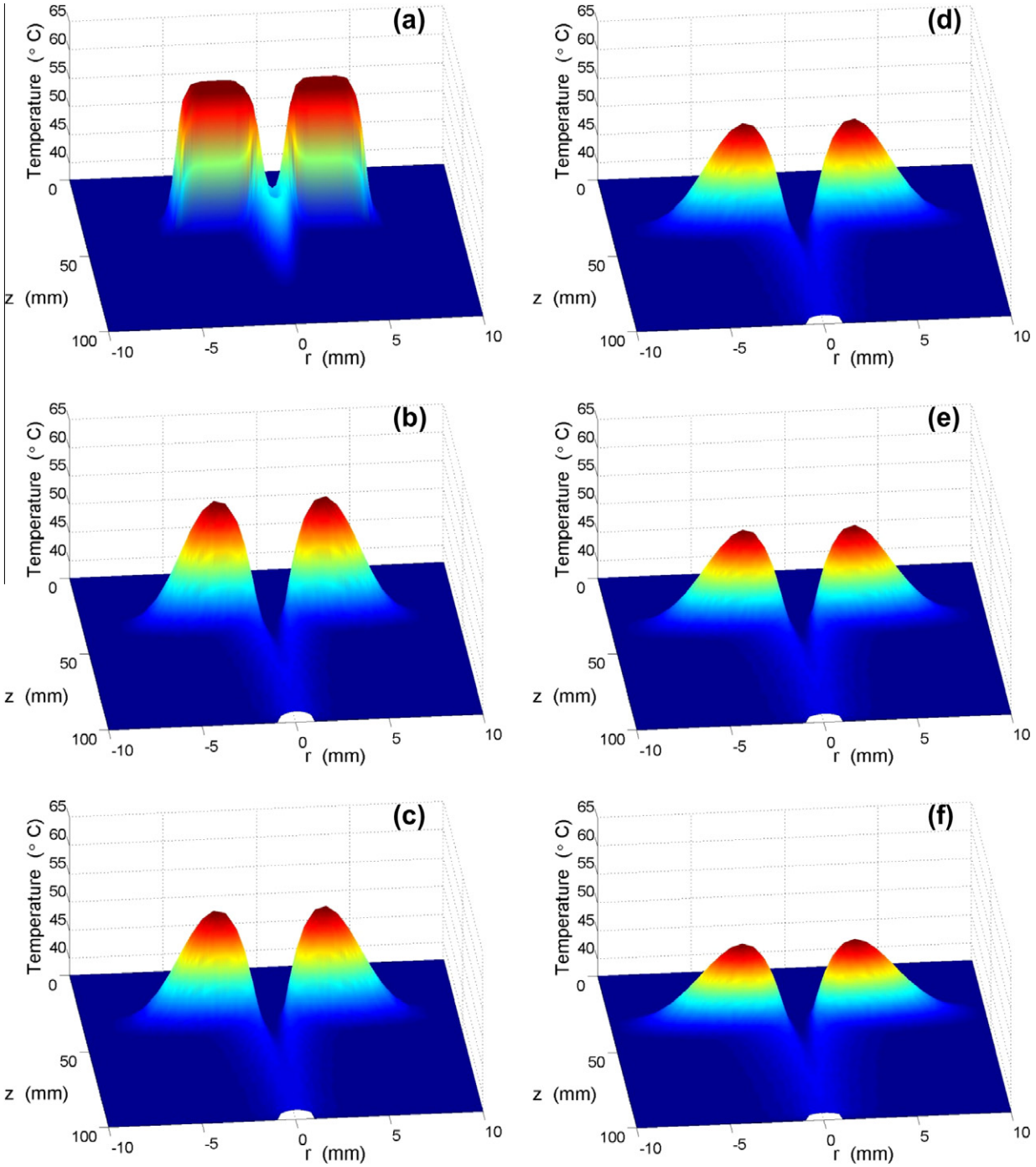

Fig. 4. Time development of temperature distribution in space for $\tau_t = 0$ s under heating scheme I in Table 2 is shown at (a) $t = 1$ s, (b) $t = 7.5$ s, (c) $t = 10$ s, (d) $t = 12$ s, (e) $t = 14.5$ s, (f) $t = 19.5$ s. The blood vessel diameter is 2 mm with the pulsation frequency being 2 Hz and amplitude factor $fac = 0.5$.

the specified error tolerance, and numerical time-stability is also automatically assured.

Owing to the heterogeneity of imposed governing equations, thermal properties, and heating, the computational domain is decomposed to 9 blocks (with meshes described below) as shown in Fig. 3. Blocks 1, 2, 3 are the blood vessel; block 5 is tumor; the others are normal tissue. Heating zones are blocks 2 and 5. We then spatially discretize the governing equations with the associated boundary/interface conditions in each block by the Chebyshev pesudospectral method [55–57], and the main work is to approximate the spatial derivatives of T_t and T_b at specially designed mesh points (called collocation points) by the Chebyshev pseudospectral method. To illustrate this, here we take a single-variable function $f(x)$, $-1 \leqslant x \leqslant 1$, as an example. $f(x)$ can be approximated by a Nth degree interpolation polynomial with exponential order of accuracy through

$$f(x) \approx f_N(x) = \sum_{j=0}^{N} f(x_j) l_j(x), \tag{21}$$

where $l_j(x)$ is the Nth degree Lagrange interpolation polynomial and $x_j = \cos(j\pi/N)$, $j = 0, 1, \ldots, N$, are specialized interpolation nodes

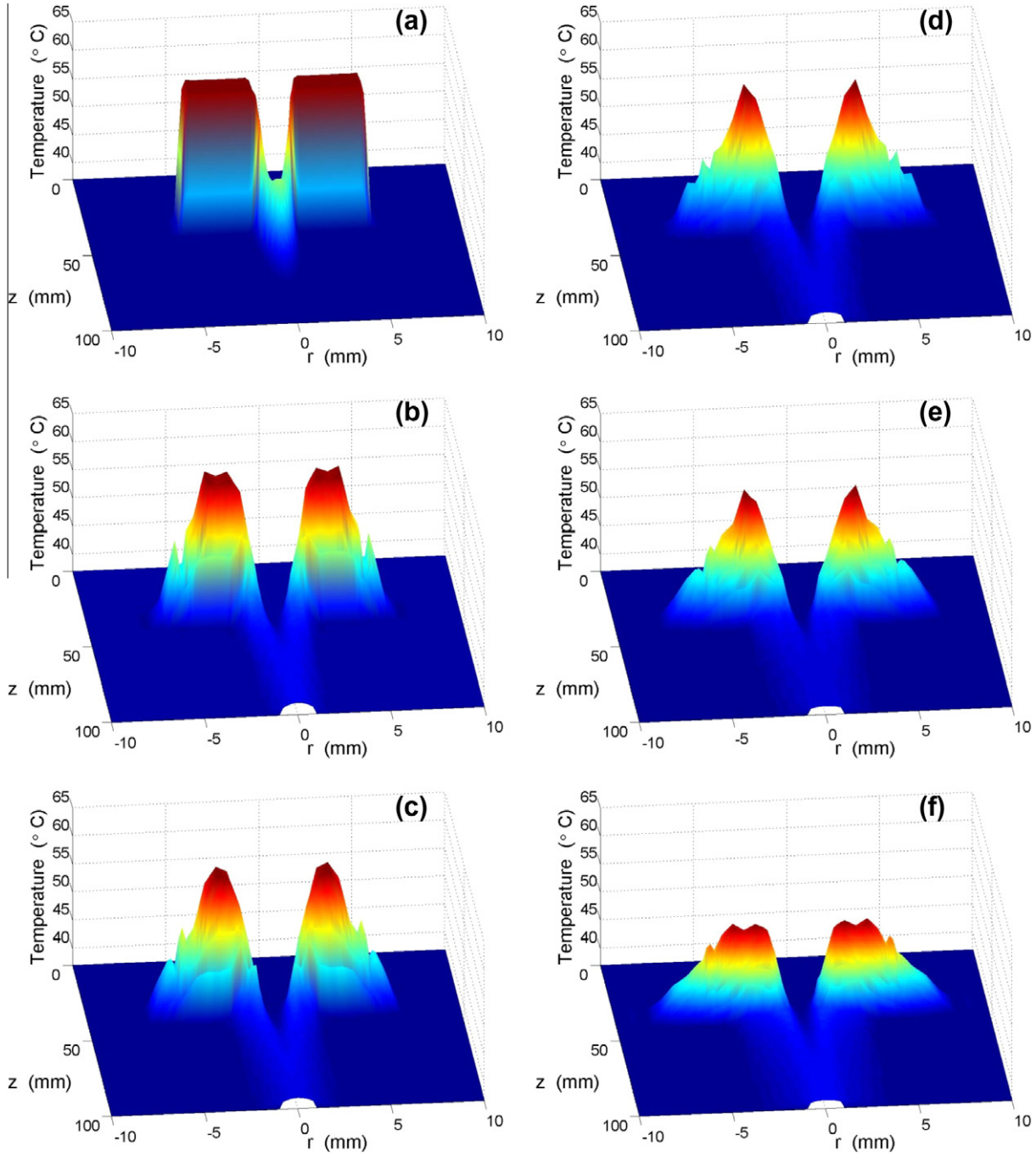

Fig. 5. Time development of temperature distribution in space for $\tau_t = 6.825$ s under heating scheme I in Table 2 is shown at (a) $t = 1$ s, (b) $t = 7.5$ s, (c) $t = 10$ s, (d) $t = 12$ s, (e) $t = 14.5$ s, (f) $t = 19.5$ s. The blood vessel diameter is 2 mm with the pulsation frequency being 2 Hz and amplitude factor $fac = 0.5$.

called the Chebyshev–Gauss–Lobatto (CGL) collocation points. CGL collocation points are the roots of the polynomial $L(x) = (1 - x^2)T'_N(x)$ with $T_N(x)$ denoting the Nth order Chebyshev polynomial. $l_j(x)$ can then be explicitly expressed as

$$l_j(x) = \frac{(-1)^{j+1}(1-x^2)T'_N(x)}{\bar{c}_j N^2 (x - x_j)}, \tag{22}$$

$$\text{with } \bar{c}_j = \begin{cases} 2, & j = 0, N, \\ 1, & j = 1, \ldots, N-1, \end{cases}$$

$$\text{such that } l_j(x_i) = \delta_{ij} = \begin{cases} 1, & i = j, \\ 0, & i \neq j. \end{cases}$$

Therefore, $\frac{df(x_i)}{dx}$ can be approximated by

$$\frac{df(x_i)}{dx} \approx \frac{df_N(x_i)}{dx} = \sum_{j=0}^{N} f(x_j) l'_j(x_i) = \sum_{j=0}^{N} D_{ij} f(x_j), \tag{23}$$

where $D_{ij} = l'_j(x_i)$ is the associated collocation derivative matrix expressed as

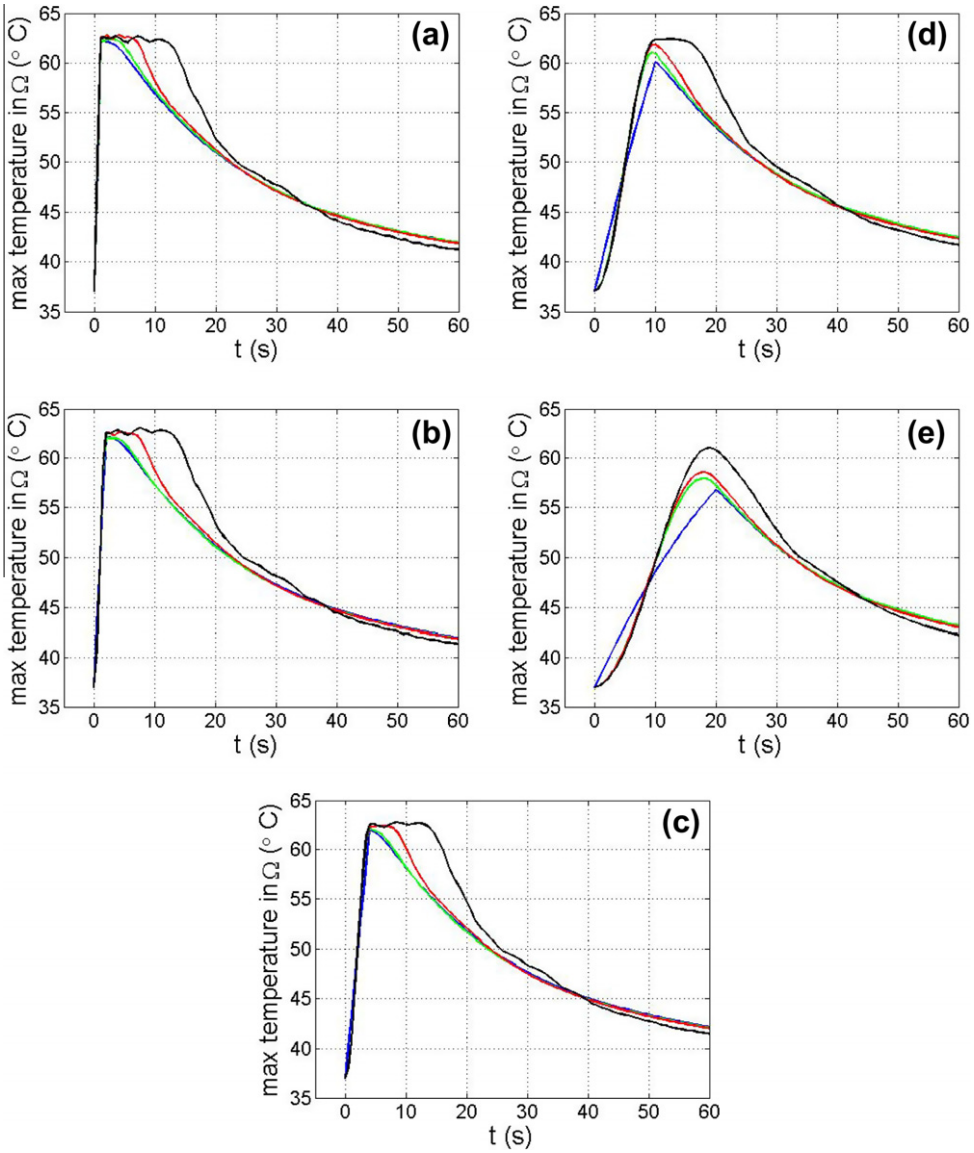

Fig. 6. Maximum temperature in space $\max_{(r,z)\in\Omega} T$ versus time with heating schemes I–V in Table 2 shown in (a)–(e) respectively. $\tau_t = 0$, 0.464, 1.756 and 6.825 s are represented by blue, green, red, and black curves respectively. The blood vessel diameter is 2 mm with the pulsation frequency being 2 Hz and amplitude factor $fac = 0.5$. (For interpretation of the references to colour in this figure legend, the reader is referred to the web version of this article.)

$$D_{ij} = \begin{cases} \frac{\bar{c}_i}{\bar{c}_j}\frac{(-1)^{i+j}}{x_i - x_j}, & i \neq j, \\ -\frac{x_j}{2(1-x_j^2)}, & 1 \leqslant i = j \leqslant N-1, \\ \frac{2N^2+1}{6}, & i = j = 0, \\ -\frac{2N^2+1}{6}, & i = j = N. \end{cases} \tag{24}$$

Similarly, higher derivatives $\frac{d^k f(x_i)}{dx^k}$ can be approximated by

$$\frac{d^k f(x_i)}{dx^k} \approx \frac{d^k f_N(x_i)}{dx^k} = \sum_{j=0}^{N} (D^k)_{ij} f(x_j). \tag{25}$$

For a multi-variable function $f(x,y)$, $-1 \leqslant x, y \leqslant 1$, it can be similarly approximated by

$$f(x,y) \approx f_{N_x,N_y}(x,y) = \sum_{j=0}^{N_x}\sum_{k=0}^{N_y} f(x_j, y_k) l_j(x) l_k(y), \tag{26}$$

which is merely a tensor-product extension of Eq. (21) with N_x degree interpolation polynomial in x direction, and N_y degree interpolation polynomial in y direction respectively. Following Eq. (25), the mth partial derivative in x direction can then be approximated by

$$\frac{\partial^m f(x_i, y_j)}{\partial x^m} \approx \frac{\partial^m f_{N_x N_y}(x_i, y_j)}{\partial x^m} = \sum_{k=0}^{N_x} (D_{N_x}^m)_{ik} f(x_k, y_j), \tag{27}$$

where D_{N_x} is basically D in Eq. (24) with $N = N_x$.

Likewise, the mth partial derivative in y direction can be approximated by

$$\frac{\partial^m f(x_i, y_j)}{\partial y^m} \approx \frac{\partial^m f_{N_x N_y}(x_i, y_j)}{\partial y^m} = \sum_{k=0}^{N_y} (D_{N_y}^m)_{jk} f(x_i, y_k), \tag{28}$$

where D_{N_y} is D in Eq. (24) with $N = N_y$ similarly.

CGL collocation points are clustered more densely near boundary, and this makes our current computational mesh more densely distributed near boundaries and interfaces as shown in Fig. 3, which is more advantageous than uniform meshes since CGL collocation points resolve boundary/interface layers more efficiently. Actually, quite economic grids were used here due to this boundary/interface layers resolving advantage and intrinsic

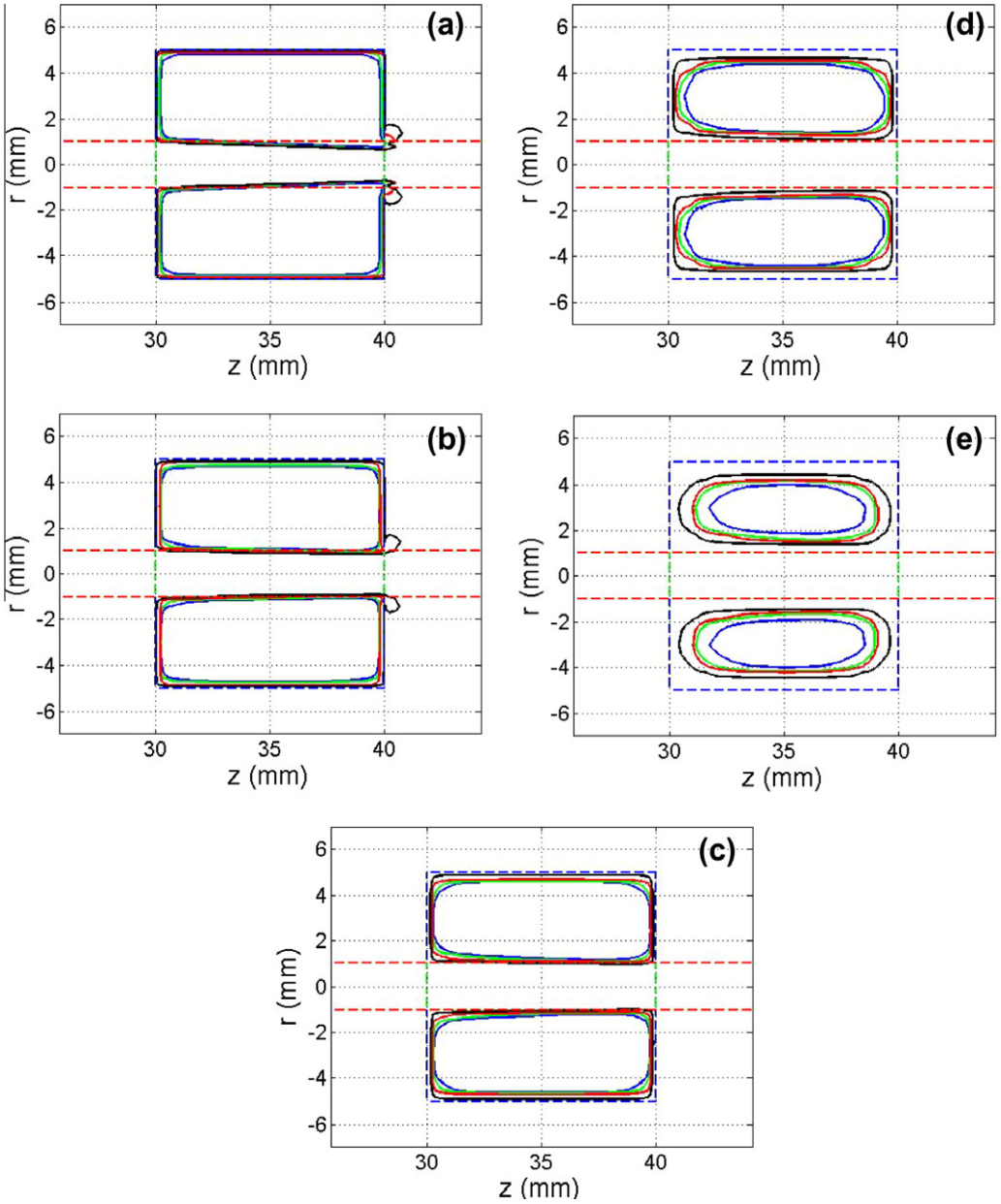

Fig. 7. Thermal lesion region represented by EM_{43} = 240 min contour with heating schemes I–V in Table 2 shown in (a)–(e) respectively. τ_t = 0, 0.464, 1.756 and 6.825 s are represented by blue, green, red, and black curves respectively. The region surrounded by blue dash line is tumor tissue (zone 5 in Fig. 2), and the one surrounded by red dash line is blood vessel. The blood vessel diameter is 2 mm with the pulsation frequency being 2 Hz and amplitude factor *fac* = 0.5. (For interpretation of the references to colour in this figure legend, the reader is referred to the web version of this article.)

high accuracy in the Chebyshev pseudospectral method, and therefore the computation efficiency is very high [58,59]. A typical set of numbers of grids used here are $N_r = \{10, 10, 10\}$ for blocks along r direction and $N_z = \{30, 10, 50\}$ for blocks along z direction, and the numerical results based on this shown in next section are all confirmed to be grid-independent ones with error of convergence generally less than 10^{-4}.

3. Results and discussions

Here we study how the thermal relaxation time τ_t, characterizing the strength of wave feature in WBTE (Eq. (13)), affect the thermal treatment. Numerical experiments were conducted under exhausted combinations of heating speed (as listed in Table 2), thermal relaxation time (τ_t = 0, 0.464, 1.756, and 6.825 s as suggested in [52]), and pulsation frequency of blood flow (1 and 2 Hz). Here we only consider the case of blood vessel diameter being 2 mm in Table 1, since larger blood vessels have been proved to be more thermally significant with sensitivity to heating speed [39]. Time evolution of maximum temperature and thermal dose are particularly chosen here to demonstrate the effect of thermal relaxation time. First we found that the difference of oscillation frequency in blood flow made tiny difference both in the maximum temperature evolution and thermal dose for all heating speeds and τ_t. We can then conclude that the thermal behavior is quite insensitive to pulsation frequency of blood flow in current study. The wave feature in WBTE (Eq. (13)) with large τ_t is found to be most pronounced when heating speed is fast. In Figs. 4 and 5, we compare the temperature evolution for τ_t = 0 and 6.825 s under the case of fastest heating speed (heating scheme I in Table 2). Non-smooth temperature distribution in space is clearly observed during time evolution, featuring strong wave propagating

behavior, in Fig. 5 for $\tau_t = 6.825$ s, while only smooth temperature distribution is observed all the time, featuring parabolicity of PBTE (Eq. (11)), in Fig. 4 for $\tau_t = 0$ s.

Time evolution of maximum temperature in space $\max_{(r,z)\in\Omega} T$ can particularly demonstrate the effect of thermal relaxation time under different heating speeds as shown in Fig. 6. Generally, this maximum temperature happens near the center of zone 5 (tumor tissue) in Fig. 2. For $\tau_t = 0$, we can see $\max_{(r,z)\in\Omega} T$ always reaches its maximum in time right at end of heating as expected, while $\max_{(r,z)\in\Omega} T$ generally exhibits plateau in time after end of heating for non-zero τ_t's, which is more pronounced as τ_t is large and heating speed is fast as comparing sub-figures in Fig. 6. This can be easily understood by the fact that heat transfer is slower (takes more time to relax) at large τ_t and high temperature tends to accumulate and preserve in time at tumor zone when heating is fast (less time for tumor to respond and relax thermally). However, for slow heating in Fig. 6(d, e), no plateau is observed and this may be due to the reason that heating is so slow that tumor has enough time to respond and relax thermally. In this case, we can also observe non-zero τ_t's even lead $\tau_t = 0$ to reach maximum in time for $\max_{(r,z)\in\Omega} T$. Besides, $\max_{(r,z)\in\Omega} T$ reaches its maximum in time with larger maximum when τ_t is larger.

The accumulated thermal dose to tissue is a function of heating duration and the temperature level [60]. The estimate of tissue damage is based on the thermal dose of which the formula was proposed by Sapareto and Dewey [61]. The thermal dose or equivalent minutes at 43 °C (EM_{43}) is shown as follows:

$$EM_{43}(\text{in min.}) = \int_0^{t_f} R^{T-43} dt, \tag{29}$$

where $R = 2$ for $T \geqslant 43$ °C, $R = 4$ for 37 °C $< T <$ 43 °C, and $t_f = 60$ s in current study. The threshold dose for necrosis is $EM_{43} = 240$ min for muscle tissue, and the region encircled by the level curve $EM_{43} = 240$ min is taken as the thermal lesion region. Covering tumor tissue but not normal tissue by thermal lesion region as full as possible is most desired in the thermal treatment. From Fig. 7, we can observe tumor tissue is generally covered better by thermal lesion region based on $EM_{43} = 240$ min level curve when heating is fast, and this effect is further enhanced when τ_t is large. Some even cover a small part of normal tissue near the downstream junction of blood vessel, tumor and normal tissue as shown in Fig. 7(a, b), which is actually not desired in thermal treatment. The phenomenon above is comprehensible from the fact that high temperature is preserved longer and heat is drained more slowly when heating is fast and τ_t is large as demonstrated in Fig. 6. The traditional simulations based on PBTE may under-estimate thermal lesion region since thermal relaxation time τ_t is actually non-trivial in living tissues.

4. Conclusion

A coupling model of thermal wave bioheat transfer in solid tissues and pulsatile blood flow in thermal significant blood vessels has been developed and studied with various combinations of heating speed, thermal relaxation time, and pulsation frequency of blood flow. Though the pulsation frequency from heart beat would affect the velocity profile of blood flow largely and exhibit flat-top and two-peak shapes in oscillatory component of velocity profile when frequency is large, it seems that the thermal behavior is quite insensitive to pulsation frequency here. Nevertheless, the thermal behavior is found to be very sensitive to the heating speed and thermal relaxation time in the current study. Heat drains more slowly and tumor tissue preserves high temperature longer when heating is fast and thermal relaxation time is large. This is all due to the wave feature characterized by large thermal relaxation time, and would cause the thermal lesion region based on $EM_{43} = 240$ min level curve to cover the tumor region better. It implies that the traditional simulations based on PBTE may under-estimate thermal dose since thermal relaxation time is actually non-trivial in living tissues.

Acknowledgments

This research was sponsored in part by the National Science Council of the Republic of China under Grant No. NSC-98-2221-E-039-001 (Dr. Shih), No. NSC-99-2221-E-039-011 (Dr. Shih), NSC-100-2221-E-039-002-MY3 (Dr. Shih), NSC-100-2115-M-035-001 (Dr. Horng) and partially by the China Medical University project No. CMU98-S-49 (Dr. Shih).

References

[1] R.B. Roemer, Engineering aspects of hyperthermia therapy, Annu. Rev. Biomed. Eng. 1 (1999) 347–376.
[2] P. Wust, B. Hildebrandt, G. Sreenivasa, B. Rau, J. Gellermann, H. Riess, R. Felix, P.M. Schlag, Hyperthermia in combined treatment of cancer, Lancet Oncol. 3 (2002) 487–497.
[3] W.C. Dewey, Arrhenius relationships from the molecule and cell to the clinic, Int. J. Hyperthermia 25 (2009) 3–20.
[4] B. Decadt, A.K. Siriwardena, Radiofrequency ablation of liver tumours: systematic review, Lancet Oncol. 5 (2004) 550–560.
[5] N.T. Wright, J.D. Humphrey, Denaturation of collagen via heating: an irreversible rate process, Annu. Rev. Biomed. Eng. 4 (2002) 109–128.
[6] C.J. Diederich, Thermal ablation and high-temperature thermal therapy: overview of technology and clinical implementation, Int. J. Hyperthermia 21 (2005) 745–753.
[7] F.A. Jolesz, MRI-guided focused ultrasound surgery, Annu. Rev. Med. 60 (2009) 417–430.
[8] J.A. López Molina, M.J. Rivera, M. Trujillo, Thermal modeling for pulsed radiofrequency ablation: analytical study based on hyperbolic heat conduction, Med. Phys. 36 (2009) 1112–1119.
[9] H.I. Vargas, W.C. Dooley, R.A. Gardner, K.D. Gonzalez, R. Venegas, S.H. Heywang-Kobrunner, A.J. Fenn, Focused microwave phased array thermotherapy for ablation of early-stage breast cancer: results of thermal dose escalation, Ann. Surgical Oncol. 11 (2004) 139–146.
[10] A. Narasimhan, K.K. Jha, L. Gopal, Transient simulations of heat transfer in human eye undergoing laser surgery, Int. J. Heat Mass Transfer 53 (2010) 482–490.
[11] M. Jaunich, S. Raje, K. Kim, K. Mitra, Z. Guo, Bio-heat transfer analysis during short pulse laser irradiation of tissues, Int. J. Heat Mass Transfer 51 (2008) 5511–5521.
[12] H.H. Pennes, Analysis of tissue and arterial blood temperature in the resting human forearm, J. Appl. Physiol. 1 (1948) 93–122.
[13] D.A. Nelson, Invited editorial on "Pennes' 1948 paper revisited", J. Appl. Physiol. 85 (1998) 2–3.
[14] A. Nakayama, F. Kuwahara, A general bioheat transfer model based on the theory of porous media, Int. J. Heat Mass Transfer 51 (2008) 3190–3199.
[15] S. Mahjoob, K. Vafai, Analytical characterization of heat transport through biological media incorporating hyperthermia treatment, Int. J. Heat Mass Transfer 53 (2010) 482–490.
[16] D. Shrivastava, J.T. Vaughan, A generic bioheat transfer thermal model for a perfused tissue, J. Biomech. Eng. 131 (2009) 1–12.
[17] K.R. Diller, Bioheat and mass transfer as viewed through a microscope, ASME J. Biomech. Eng. 127 (2005) 67–84.
[18] M.C. Kolios, M.D. Sherar, J.W. Hunt, Blood flow cooling and ultrasonic lesion formation, Med. Phys. 23 (1996) 1287–1298.
[19] A. Kotte, G. van Leeuwen, J. de Bree, J. van der Koijk, H. Crezee, J. Lagendjik, A description of discrete vessel segments in thermal modeling of tissues, Phys. Med. Biol. 41 (1996) 865–884.
[20] J.C. Chato, Heat transfer to blood vessels, J. Biomech. Eng. 102 (1980) 110–118.
[21] J.J.W. Lagendijk, The influence of bloodflow in large vessels on the temperature distribution in hyperthermia, Phys. Med. Biol. 27 (1982) 17–23.
[22] J. Crezee, J.J.W. Lagendijk, Temperature uniformity during hyperthermia: the impact of large vessels, Phys. Med. Biol. 37 (1992) 1321–1337.
[23] P. Hariharan, M.R. Myers, R.K. Banerjee, HIFU procedures at moderate intensities-effect of large blood vessels, Phys. Med. Biol. 52 (2007) 3493–3513.
[24] L. Consiglieri, I. dos Santos, D. Haemmerich, Theoretical analysis of the heat convection coefficient in large vessels and the significance for thermal ablative therapies, Phys. Med. Biol. 48 (2003) 4125–4134.
[25] D. Shrivastava, R.B. Roemer, Readdressing the issue of thermally significant blood vessels using a countercurrent vessel network, ASME J. Biomech. Eng. 128 (2006) 210–216.
[26] Q. He, L. Zhu, D.E. Lemonds, S. Weinbaum, Experimental measurements of the temperature variation along artery-vein pairs from 200 to 1000 μm diameter in rat hind limb, ASME J. Biomech. Eng. 124 (2002) 656–661.

[27] D.A. McDonald, The relation of pulsatile pressure to flow in arteries, J. Physiol. 127 (1955) 533–552.
[28] R. Kelly, C. Hayward, A. Avolio, M. O'Rourke, Noninvasive determination of age-related changes in the human arterial pulse, Circulation 80 (1989) 1652–1659.
[29] M. Zamir, The Physics of Coronary Blood Flow, Springer-Verlag, New York, 2005.
[30] D.N. Ku, Blood flow in arteries, Annu. Rev. Fluid Mech. 29 (1997) 399–434.
[31] J.R. Womersley, Method for the calculation of velocity, rate of flow and viscous drag in arteries when the pressure gradient is know, J. Physiol. 127 (1955) 553–563.
[32] C. Loudon, A. Tordesillas, The use of the dimensionless Womersley number to characterize the unsteady nature of internal flow, J. Theor. Biol. 191 (1998) 63–78.
[33] T.C. Shih, H.S. Kou, W.L. Lin, Cooling effect of thermally significant blood vessels in perfused tumor tissue during thermal therapy, Int. Commun. Heat Mass Transfer 33 (2006) 135–141.
[34] M.C. Kolios, M.D. Sherar, J.W. Hunt, Large blood vessel cooling in heated tissues: a numerical study, Phys. Med. Phys. 40 (1995) 477–494.
[35] T.C. Shih, H.S. Kou, W.L. Lin, The impact of thermally significant blood vessels in perfused tumor tissue on thermal distributions during thermal therapies, Int. Commun. Heat Mass Transfer 30 (2003) 975–985.
[36] K. Khanafer, J.L. Bull, I. Pop, R. Berguer, Influence of pulsatile blood flow and heating scheme on the temperature distribution during hyperthermia treatment, Int. J. Heat Mass Transfer 50 (2007) 4883–4890.
[37] C.W. Song, A. Lokshina, J.G. Rhee, M. Paten, S.H. Levitt, Implication of blood flow in hyperthermia treatments of tumors, IEEE Trans. Biomed. Eng. BME-31 (1984) 9–16.
[38] O.I. Craciunescu, S.T. Clegg, Pulsatile blood flow effects on temperature distribution and heat transfer in rigid vessels, ASME J. Biomech. Eng. 123 (2001) 500–505.
[39] T.L. Horng, W.L. Lin, C.T. Liauh, T.C. Shih, Effects of pulsatile blood flow in large vessels on thermal dose distribution during thermal therapy, Med. Phys. 34 (2007) 1312–1320.
[40] D.D. Joseph, L. Preziosi, Heat waves, Rev. Mod. Phys. 61 (1989) 41–73.
[41] M.N. Özisik, D.Y. Tzou, On the wave theory in heat conduction, ASME Trans. J. Heat Transfer 116 (1994) 525–526.
[42] D.Y. Tzou, Marco to Micro-scale Heat Transfer: The Lagging Behavior, Taylor and Francis, Washington, DC, 1997.
[43] K. Kaminski, Hyperbolic heat conduction equation for materials with a nonhomogeneous inner structure, ASME Trans. J. Heat Transfer 112 (1990) 555–560.
[44] J. Zhou, Y. Zhang, J.K. Chen, Non-Fourier heat conduction effect on laser-induced thermal damage in biological tissues, Numer. Heat Tr. 54 (2008) 1–19.
[45] J. Zhou, J.K. Chen, Y. Zhang, Dual-phase effects on thermal damage to biological tissues caused by laser irradiation, Computer Biol. Med. 39 (2009) 286–293.
[46] R.B. Roemer, J.R. Oleson, T.C. Cetas, Oscillatory temperature response to constant power applied to canine muscle, Am. J. Physiol. 249 (1985) R153–R158.
[47] K. Mitra, S. Kumar, A. Vedavarz, M.K. Moallemin, Experimental evidence of hyperbolic heat conduction in processed meat, ASME Trans. J. Heat Transfer 117 (1995) 568–573.
[48] P.J. Antaki, New interpretation of non-Fourier heat conduction in processed meat, ASME Trans. J. Heat Transfer 127 (2005) 189–193.
[49] C. Cattaneo, Sur une forme de l'équation de la chaleur éliminant le paradoxe d'une propagation instantaneé, Comptes Rendus 247 (1958) 431–433.
[50] P. Vernotte, Les paradoxes de la théorie continue de l'équation de la chaleur, Comptes Rendus 246 (1958) 3154–3155.
[51] W. Roetzel, N. Putra, S.K. Das, Experiment and analysis for non-Fourier conduction in materials with non-homogeneous inner structure, Int. J. Thermal Sci. 42 (2003) 541–552.
[52] Y. Zhang, Generalized dual-phase lag bioheat equations based on non-equilibrium heat transfer in living biological tissues, Int. J. Heat Mass Transfer 52 (2009) 4829–4834.
[53] W.W. Nichols, M.F. O'Rourke, McDonald's Blood Flow in Arteries: Theoretic, Experimental and Clinical Principles, Lea & Febiger, Philadelphia, 1990.
[54] Y. Huo, G.S. Kasab, Pulsatile blood flow in the entire coronary arterial tree: theory and experiment, Am. J. Physiol. Heart Circ. Physiol. 291 (2006) H1074–H1087.
[55] C. Canuto, M.Y. Hussaini, A. Quarteroni, T.A. Zhang, Spectral Methods, Fundamentals in Single Domains, Springer-Verlag, Berlin, Heidelberg, 2006.
[56] L.N. Trefethen, Spectral Methods in Matlab, SIAM, Philadelphia, 2000.
[57] B. Fornberg, A Practical Guide to Pseudospectral Methods, Cambridge University Press, Cambridge, 1996.
[58] J. Hou, B. Guo, Chebyshev pseudospectral-finite element method for the three-dimensional unsteady Naier-Stokes equation, Appl. Math. Comput. 101 (1999) 209–244.
[59] J. Lee, Q.H. Liu, An efficient 3D spectral-element method for Schrodinger equation in nanodevice simulation, IEEE T. Comput. Aid. D. 24 (2005) 1848–1858.
[60] H.S. Kou, T.C. Shih, W.L. Lin, Effect of directional blood flow on thermal dose distribution during thermal therapy: an application of Green's function based on the porous model, Phys. Med. Biol. 48 (2003) 1577–1589.
[61] S.A. Sapareto, W.C. Dewey, Thermal dose determination in cancer therapy, Int. J. Radiat. Oncol., Biol., Phys 10 (1984) 787–800.